

A three-dimensional map of the Milky Way using classical Cepheid variable stars

Dorota M. Skowron,^{1,*} Jan Skowron,¹ Przemek Mróz,¹ Andrzej Udalski,^{1*}
Paweł Pietrukowicz,¹ Igor Soszyński,¹ Michał K. Szymański,¹
Radosław Poleski,^{1,2} Szymon Kozłowski,¹ Krzysztof Ulaczyk,^{1,3}
Krzysztof Rybicki,¹ Patryk Iwanek¹

¹Astronomical Observatory, University of Warsaw,
Aleje Ujazdowskie 4, 00-478 Warsaw, Poland,

²Department of Astronomy, Ohio State University,
140 W. 18th Ave., Columbus, OH 43210, USA

³Department of Physics, University of Warwick, Coventry CV4 7AL, UK

*E-mail: dszczyg@astrouw.edu.pl, udalski@astrouw.edu.pl

July 18, 2019; submitted: May 29, 2018

The Milky Way is a barred spiral galaxy, with physical properties inferred from various tracers informed by the extrapolation of structures seen in other galaxies. However, the distances of these tracers are measured indirectly and are model-dependent. We constructed a map of the Milky Way in three-dimensions based on the positions and distances of thousands of classical Cepheid variable stars. This map shows the structure of our Galaxy's young stellar population, and allows us to constrain the warped shape of the Milky Way's disk. A simple model of star formation in the spiral arms reproduces the observed distribution of Cepheids.

Cepheid variable stars pulsate, causing their brightness to vary with periods of 1 to 100 days. Classical Cepheids are young (< 400 million years old) supergiant stars, whereas other types of Cepheids (type II and anomalous) arise in older stellar populations. The intrinsic luminosities of classical Cepheids span the range of 100 to 10,000 solar luminosities (L_{\odot}). This is bright enough to be detected at extragalactic distances and, within our Galaxy, through obscuring interstellar clouds of gas and dust in the foreground. Cepheids follow a pulsation period-luminosity (P-L) relation (*I*), allowing the absolute magnitude of a Cepheid to be inferred from its period. The distance can then be determined by comparing the absolute and the apparent magnitude, provided the foreground interstellar extinction is known. At optical wavelengths, interstellar extinction is often large and highly variable, but observations in infrared (IR) bands reduce these uncertainties. Detection of Cepheids in the optical bands is straightforward owing to their characteristic saw-tooth shaped light curves and large amplitudes. In the IR, the light curve shape becomes more sinusoidal and difficult to distinguish from other types of variable stars. Cepheids can appear indistinguishable from other variable stars in the optical bands if the number of measurements is limited (below 80 to 100 epochs) and the survey time span is short.

We analyzed data for 2431 Galactic Cepheids, most of which were discovered by the fourth phase of the Optical Gravitational Lensing Experiment (OGLE-IV) project (2). This is a long-term survey of the Galactic disk and center focused on the discovery and classification of variable stars. The OGLE Collection of Galactic Cepheids (3) more than doubled the number of known Galactic classical Cepheids. The magnitude range of the Galactic plane portion of OGLE-IV, 11 to 18 mag in the *I*-band, enables identification of Cepheids as distant as the expected boundary of the Galactic disk ($\approx 20\,000$ parsecs (pc) from the Galactic center). OGLE has covered almost all the Galactic disk visible from its site at Las Campanas Observatory, Chile (Fig 1).

Cepheids closer than 4 kpc are too bright, so they saturate in the OGLE survey images. Therefore, we complemented the OGLE sample with brighter objects from the list of Galactic Cepheids (4), themselves mostly from the General Catalogue of Variable Stars (GCVS) (5) and the All Sky Automated Survey (ASAS) (6) survey. We also supplemented the list with Cepheids discovered by the All-Sky Automated Survey for Supernovae (ASAS-SN) survey (7) and we identified Cepheids in the Asteroid Terrestrial-impact Last Alert System (ATLAS) survey catalog (8). We also investigated Cepheid candidates from the Gaia Data Release 2 (Gaia DR2) catalog (9), confirming 211 of them as classical Cepheids. Full details on the sample selection are provided in (10).

Most of the Cepheids lie close to the Galactic plane, so they are affected by extinction by dust, which is also concentrated in the plane. To reduce the effect of dust extinction, we determined the distances to individual Cepheids based on mid-IR photometry obtained by the Spitzer and Wide-field Infrared Survey Explorer (WISE) satellites corrected for interstellar extinction (10), as well as appropriate P-L relations (11). Positions and distances of each Cepheid were converted to Cartesian coordinates with the Sun at the origin to facilitate study of their 3-D distribution (10).

Fig. 1 presents our map of the Galaxy in Cepheids, representing the young stellar population. We show the view projected on the sky (Fig. 1 A) and face-on (Fig. 1 B), together with a four-arm spiral galaxy model consistent with neutral hydrogen (H I) observations (12). Areas of higher Cepheid density indicate the non-uniform Galactic structure or regions of enhanced star formation. The side view (Fig. 1 A) shows that the young stellar disk of the Milky Way between longitudes $240^\circ < l < 330^\circ$ lies below the Galactic plane (as traced by Cepheids), suggests warping of the Galactic disk.

We subdivided the Galaxy into 12 sectors of unequal azimuthal width in the Galactocentric polar coordinate system with the azimuth $\phi = 0^\circ$ pointing to the Sun (Fig. 2 A). The disk is

not flat – the warp is evident in directions that are sufficiently well populated with Cepheids (Fig. 2 B). The warping of the disk begins at a distance of ~ 8 kpc and becomes steeper at ~ 10 kpc, reaching out to the edge of the Galaxy at ~ 20 kpc. The disk warps toward negative distance from the Galactic plane (Z) in the azimuth range $0^\circ < \phi < 135^\circ$ and toward positive Z from $165^\circ < \phi < 330^\circ$, although the exact boundary is unclear due to the lower number of known Cepheids on the far side of the Galactic center. To further illustrate the warping of the disk and as a guide to the eye, we fitted a simple model surface to the Cepheid distribution (10), which is shown in Fig. 2 C to E from three viewing angles.

The warping of the disk has been observed before, in H I (12, 13), stars (14–18), dust (19), and kinematics of stars in the plane of the sky (20, 21). Our map shows the warp in three dimensions and differs from models derived from those earlier detections (10).

We modeled the thickness of the young disk by fitting a simple exponential model (10). We measured the disk scale height within the solar orbit $H = 73.5 \pm 3.2$ pc and the distance of the Sun from the Galactic plane $z_0 = 14.5 \pm 3.0$ pc (Fig. S3). These values can be compared to the past determinations (Table S2). We removed the average warp shape from the Galactic disk to analyze its flaring properties far from the center (Fig. S2). We found that the flaring of the disk in Cepheids matches that seen in neutral hydrogen (22) (Fig. S2 B).

The distribution of classical Cepheid pulsation periods as a function of the distance from the Galactic center is presented in Fig. S4. It shows a decrease in the minimal pulsation periods of Cepheids with the increasing Galactocentric distance consistent with a radial gradient of metallicity (abundance of elements heavier than hydrogen and helium) in the Milky Way (23–25).

The age of classical Cepheids is correlated with their pulsation period, metallicity and stellar rotation (24). Using the period distribution, we performed an age tomography of the Milky Way Cepheids (Fig. 3 A). After applying the period-age relations for Cepheids (24) and including the

metallicity gradient (10, 25), we determined that the majority of Cepheids in our sample formed between 50 million and 250 million years ago (Fig. 3 B). The spatial distribution of ages shows that the closer to the Galactic center, the younger Cepheids we observe (Fig. 3 C to E). The age distribution of Cepheids does not directly reflect that of all stars present in the disk. For example, the absence of short-period Cepheids in the inner disk does not necessarily mean that older (less massive) stars are absent in that region, as the higher metallicity there would not have produced Cepheids in the older population.

The spatial distribution of Cepheids shows several distinct features (Fig. 3 A). Because these features are located mainly in the area monitored by OGLE, where the Cepheid detection efficiency is high (3), they are most likely real, rather than the result of an observational bias. The most prominent feature is formed by Cepheids within an age range of 90 to 140 Myr (Fig. 3 D). Traces of this arc-shaped overdensity were previously associated with the Sagittarius-Carina spiral arm (26–29). An additional small overdensity in this age range is connected with the Perseus arm.

Fig. 1 B also shows additional overdensities of Cepheids. In Fig. 3 C, E we present the distribution of our Cepheids in the age ranges of 20 to 90 Myr and 140 to 260 Myr, respectively. There are three overdensities in the youngest bin and two in the oldest one. The youngest overdensities roughly correspond to the inner Galaxy spiral arms (Norma-Cygnus, Scutum-Crux-Centaurus, and Sagittarius-Carina) whereas for the oldest ones, possible associations with the Perseus and Norma-Cygnus/Outer arms are much less evident. Cepheids within individual overdensities have similar ages, suggesting a common origin in past star formation episodes.

We performed a simple simulation in which we select stars from three age bins. Median age values in these three groups were 64, 113 and 175 Myr. Then we searched for a star formation episode in one or more of the spiral arms, which, after a given time (after the Galaxy has rotated), would produce the currently observed distribution of Cepheids. The results of this

simulation are presented in Fig. 4, where each row focuses on one of the age bins.

Fig. 4, A, D, and G, shows the current observed distribution of Cepheids. Fig. 4, B, E, and H presents the positions of the spiral arms as they were 64 Myr, 113 Myr, and 175 Myr ago, respectively, following an assumed rotational period of the spiral pattern equal to 250 Myr (29). At those moments and locations, we injected star formation episodes. Fig. 4, C, F, and I, shows how those star formation regions would look now (after 64, 113, and 175 Myr, respectively), taking into account the typical velocity of disk stars (30). We require a low-velocity dispersion of Cepheids during their birth (8 km/s) to match the coherent overdensities we observe.

Even with these simple assumptions, we find a good match between the observed and simulated distributions of Cepheids in the shape of the overdensities, as well as in their internal dispersion. Cepheids that were formed in a spiral arm, do not currently follow the exact location of that arm; this can be explained by the difference in rotation velocity between the spiral density waves and the stars. This is the most pronounced in the case of the oldest group (Fig. 4 G to I), where the overdensities fall between the Perseus and Norma-Cygnus/Outer arms, in which they were most likely formed, and in the Sagittarius-Carina – Perseus arm gap.

We have produced a three-dimensional map of the Milky Way based on a large number of individual Cepheids with measured distances. This represents the young stellar population that extends to about 20 kpc, covering a large portion of our Galaxy, thus illustrating the extent and shape of the young stellar disk. Our work shows that a simple model can reproduce the current distribution of the young stellar disk of the Milky Way with narrow patches of stars of similar age.

References

1. H. S. Leavitt, E. C. Pickering, *Harvard College Observatory Circular* **173**, 1 (1912).
2. A. Udalski, M. K. Szymański, G. Szymański, *Acta Astron.* **65**, 1 (2015).
3. A. Udalski, *et al.*, *Acta Astron.* **68**, 315 (2018).
4. P. Pietrukowicz, *et al.*, *Acta Astron.* **63**, 379 (2013).
5. N. N. Samus, E. V. Kazarovets, O. V. Durlevich, N. N. Kireeva, E. N. Pastukhova, *Astronomy Reports* **61**, 80 (2017).
6. G. Pojmański, *Acta Astron.* **52**, 397 (2002).
7. T. Jayasinghe, *et al.*, *Mon. Not. R. Astron. Soc.* **477**, 3145 (2018).
8. A. N. Heinze, *et al.*, *Astron. J.* **156**, 241 (2018).
9. B. Holl, *et al.*, *Astron. Astrophys.* **618**, A30 (2018).
10. Materials and methods are available as supplementary materials.
11. S. Wang, X. Chen, R. de Grijs, L. Deng, *Astrophys. J.* **852**, 78 (2018).
12. E. S. Levine, L. Blitz, C. Heiles, *Science* **312**, 1773 (2006).
13. H. Nakanishi, Y. Sofue, *Publ. Astron. Soc. Jpn.* **55**, 191 (2003).
14. R. Drimmel, D. N. Spergel, *Astrophys. J.* **556**, 181 (2001).
15. M. López-Corredoira, A. Cabrera-Lavers, F. Garzón, P. L. Hammersley, *Astron. Astrophys.* **394**, 883 (2002).
16. Y. Momany, *et al.*, *Astron. Astrophys.* **451**, 515 (2006).

17. C. Reylé, D. J. Marshall, A. C. Robin, M. Schultheis, *Astron. Astrophys.* **495**, 819 (2009).
18. E. B. Amôres, A. C. Robin, C. Reylé, *Astron. Astrophys.* **602**, A67 (2017).
19. D. J. Marshall, A. C. Robin, C. Reylé, M. Schultheis, S. Picaud, *Astron. Astrophys.* **453**, 635 (2006).
20. R. L. Smart, R. Drimmel, M. G. Lattanzi, J. J. Binney, *Nature* **392**, 471 (1998).
21. E. Poggio, *et al.*, *Mon. Not. R. Astron. Soc.* **481**, L21 (2018).
22. P. M. W. Kalberla, L. Dedes, J. Kerp, U. Haud, *Astron. Astrophys.* **469**, 511 (2007).
23. E. Antonello, D. Fugazza, L. Mantegazza, M. Stefanon, S. Covino, *Astron. Astrophys.* **386**, 860 (2002).
24. R. I. Anderson, H. Saio, S. Ekström, C. Georgy, G. Meynet, *Astron. Astrophys.* **591**, A8 (2016).
25. K. Genovali, *et al.*, *Astron. Astrophys.* **566**, A37 (2014).
26. D. J. Majaess, D. G. Turner, D. J. Lane, *Mon. Not. R. Astron. Soc.* **398**, 263 (2009).
27. A. K. Dambis, *et al.*, *Astronomy Letters* **41**, 489 (2015).
28. A. Sanna, M. J. Reid, T. M. Dame, K. M. Menten, A. Brunthaler, *Science* **358**, 227 (2017).
29. J. P. Vallée, *The Astronomical Review* **13**, 113 (2017).
30. P. Mróz, *et al.*, *Astrophys. J.* **870**, L10 (2019).
31. I. Soszyński, *et al.*, *Acta Astron.* **67**, 297 (2017).
32. I. Soszyński, *et al.*, *Acta Astron.* **61**, 285 (2011).

33. I. Soszyński, *et al.*, *Acta Astron.* **58**, 163 (2008).
34. E. L. Wright, *et al.*, *Astron. J.* **140**, 1868 (2010).
35. A. Mainzer, *et al.*, *Astrophys. J.* **731**, 53 (2011).
36. P. Klagyivik, L. Szabados, *Astron. Astrophys.* **504**, 959 (2009).
37. R. A. Benjamin, *et al.*, *Publ. Astron. Soc. Pac.* **115**, 953 (2003).
38. E. Churchwell, *et al.*, *Publ. Astron. Soc. Pac.* **121**, 213 (2009).
39. J. Bovy, H.-W. Rix, G. M. Green, E. F. Schlafly, D. P. Finkbeiner, *Astrophys. J.* **818**, 130 (2016).
40. G. M. Green, *et al.*, *Astrophys. J.* **810**, 25 (2015).
41. R. K. Saito, *et al.*, *Astron. Astrophys.* **537**, A107 (2012).
42. M. Xue, *et al.*, *Astrophys. J. Suppl. Ser.* **224**, 23 (2016).
43. Gaia Collaboration, *et al.*, *Astron. Astrophys.* **616**, A1 (2018).
44. A. G. Riess, *et al.*, *Astrophys. J.* **861**, 126 (2018).
45. L. Lindegren, *et al.*, *Astron. Astrophys.* **616**, A2 (2018).
46. J. C. Zinn, M. H. Pinsonneault, D. Huber, D. Stello, *Astrophys. J.* **878**, 136 (2019).
47. K. G. Stassun, G. Torres, *Astrophys. J.* **862**, 61 (2018).
48. T. Muraveva, H. E. Delgado, G. Clementini, L. M. Sarro, A. Garofalo, *Mon. Not. R. Astron. Soc.* **481**, 1195 (2018).
49. M. W. Feast, J. W. Menzies, N. Matsunaga, P. A. Whitelock, *Nature* **509**, 342 (2014).

50. P. Pietrukowicz, *et al.*, *Astrophys. J.* **811**, 113 (2015).
51. S. Gillessen, *et al.*, *Astrophys. J.* **837**, 30 (2017).
52. I. Yusifov, *The Magnetized Interstellar Medium*, B. Uyaniker, W. Reich, R. Wielebinski, eds. (2004), pp. 165–169.
53. D. Foreman-Mackey, D. W. Hogg, D. Lang, J. Goodman, *Publ. Astron. Soc. Pac.* **125**, 306 (2013).
54. C. Georgy, *et al.*, *Astron. Astrophys.* **553**, A24 (2013).
55. R. C. Kennicutt, N. J. Evans, *Annual Review of Astronomy and Astrophysics* **50**, 531 (2012).
56. G. Bono, *et al.*, *Astrophys. J.* **621**, 966 (2005).
57. W. Huang, D. R. Gies, M. V. McSwain, *Astrophys. J.* **722**, 605 (2010).
58. J. Zorec, F. Royer, *Astron. Astrophys.* **537**, A120 (2012).
59. B.-C. Koo, *et al.*, *Publ. Astron. Soc. Pac.* **129**, 094102 (2017).
60. M. T. Karim, E. E. Mamajek, *Mon. Not. R. Astron. Soc.* **465**, 472 (2017).
61. J. M. Yao, R. N. Manchester, N. Wang, *Mon. Not. R. Astron. Soc.* **468**, 3289 (2017).
62. Y. C. Joshi, A. K. Dambis, A. K. Pandey, S. Joshi, *Astron. Astrophys.* **593**, A116 (2016).
63. V. V. Bobylev, A. T. Bajkova, *Astronomy Letters* **42**, 182 (2016).
64. V. V. Bobylev, A. T. Bajkova, *Astronomy Letters* **42**, 1 (2016).
65. S. A. Olausen, V. M. Kaspi, *Astrophys. J. Suppl. Ser.* **212**, 6 (2014).
66. A. S. M. Buckner, D. Froebrich, *Mon. Not. R. Astron. Soc.* **444**, 290 (2014).

67. J. Liu, Z. Zhu, *9th Pacific Rim Conference on Stellar Astrophysics*, S. Qain, K. Leung, L. Zhu, S. Kwok, eds. (2011), vol. 451 of *Astronomical Society of the Pacific Conference Series*, p. 339.
68. M. Jurić, *et al.*, *Astrophys. J.* **673**, 864 (2008).
69. B. Chen, *et al.*, *Astrophys. J.* **553**, 184 (2001).

Acknowledgments

We would like to thank the Reviewers for constructive comments that helped to improve the paper. This publication makes use of data products from the Wide-field Infrared Survey Explorer, which is a joint project of the University of California, Los Angeles, and the Jet Propulsion Laboratory/California Institute of Technology, funded by the NASA. This work is based in part on observations made with the Spitzer Space Telescope, which is operated by the Jet Propulsion Laboratory, California Institute of Technology under a contract with NASA.

Funding: The OGLE project has received funding from the National Science Center (NCN), Poland through grant MAESTRO 2014/14/A/ST9/00121 (A.U.). Also supported by NCN grant 2013/11/D/ST9/03445 (D.M.S.), NCN grant MAESTRO 2016/22/A/ST9/00009 (I.S.) and the Foundation for Polish Science – Program START (P.M.). **Authors contributions:** D.M.S., J.S. and P.M. analyzed, modeled and interpreted the Galactic Cepheid data. A.U. initiated, supervised the project and prepared the sample of Cepheids. P.P. and I.S. made the final verification of the sample used in this analysis. M.K.S. provided positional data for Cepheid variables. D.M.S., J.S., P.M. and A.U. prepared the manuscript. All authors collected the OGLE photometric observations and reviewed, discussed and commented on the results and on the manuscript. **Competing interests:** The authors of the manuscripts have no competing interests. **Data and materials availability:** Data for full Cepheid sample is available in Table S1 and Data S1. The

OGLE Collection of Galactic Cepheids is available at the OGLE Archive:

<http://www.astroww.edu.pl/ogle/ogle4/OCVS/>

The Python code for the simulations shown in Fig. 4 is available at

https://github.com/jskowron/galactic_cepheids

Supplementary Materials

Materials and Methods

Figs. S1–S5

Tables S1–S2

Data S1

References (31–69)

29 May 2018; accepted 5 July 2019

10.1126/science.aau3181

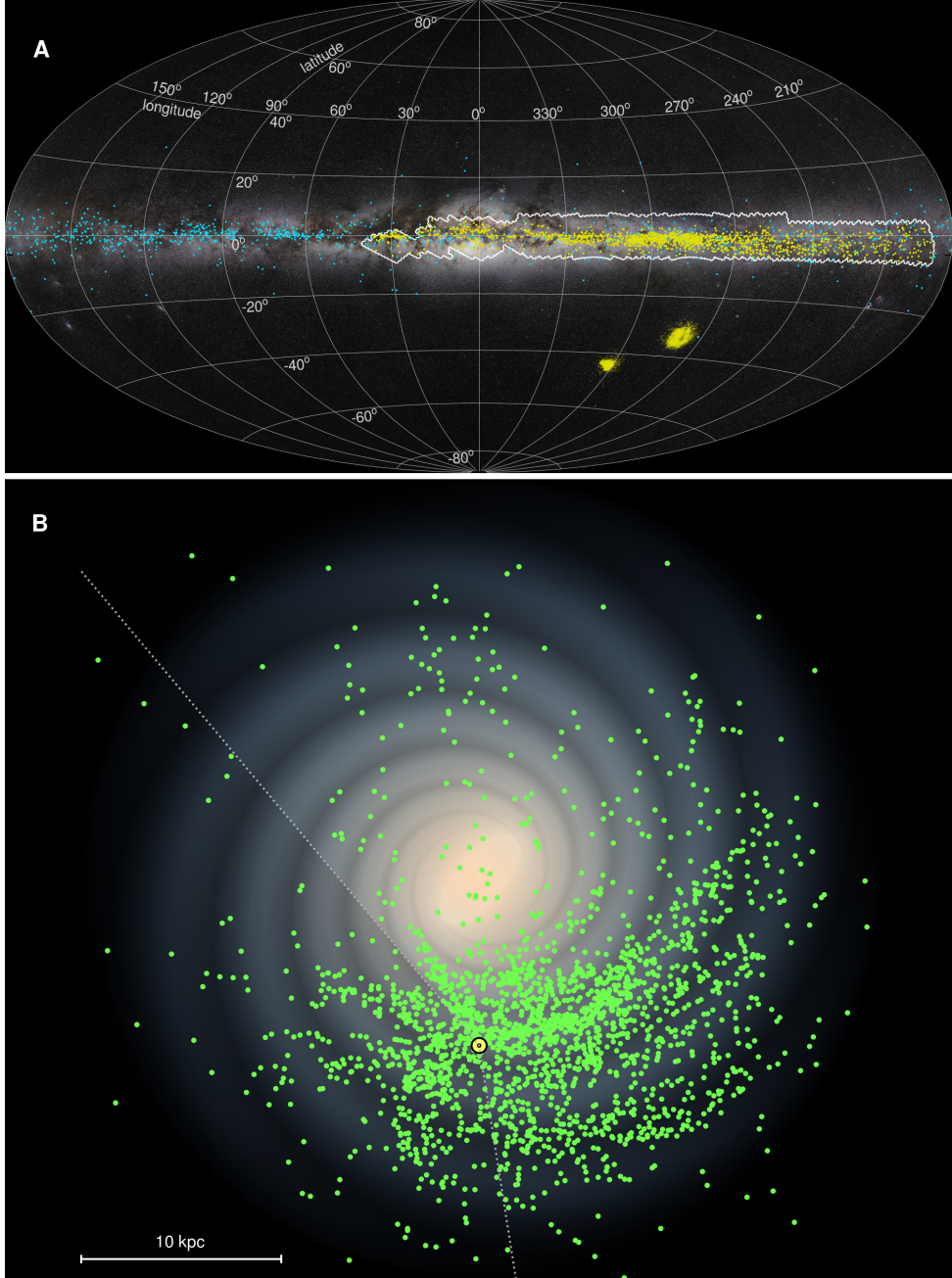


Figure 1: Distribution of Galactic classical Cepheids. (A) On-sky view of the Milky Way in Galactic coordinates (l , b), with our sample of classical Cepheids in the Milky Way and in the Magellanic Clouds. Cepheids from the OGLE Collection of Variable Stars are shown with yellow dots, other sources with cyan dots (10). The white contour marks the OGLE survey area in the Galactic plane ($190^\circ < l < 360^\circ$, $0^\circ < l < 40^\circ$; $-6^\circ < b < +6^\circ$). The background image is a Milky Way panorama (by Serge Brunier). (B) Face-on view of our Galaxy with all 2431 Cepheids in our sample marked with green dots. The background image represents a four-arm spiral galaxy model consistent with neutral hydrogen measurements in our Galaxy (with the spiral structure modeled as the logarithmic spirals (29)). The Sun is marked with a yellow dot; the dashed lines show the angular extent of the OGLE fields ($190^\circ < l < 360^\circ$, $0^\circ < l < 40^\circ$).

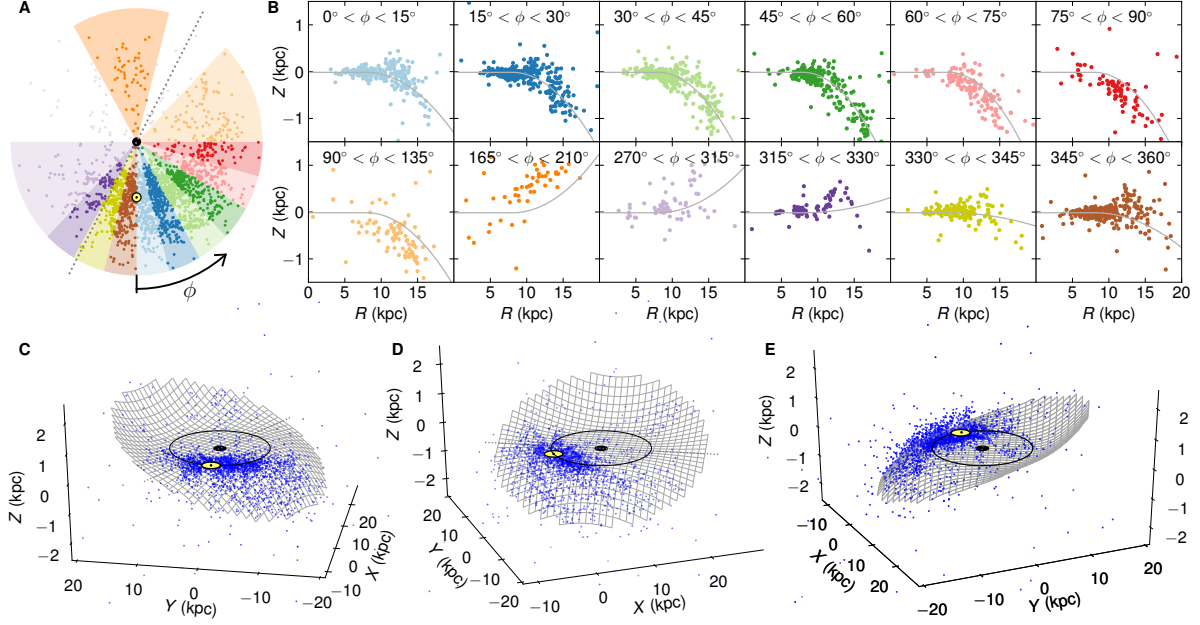


Figure 2: Warping of the Milky Way’s disk. (A) Top view of the Galactic disk divided into 12 sectors in the Galactocentric polar coordinate system. The azimuth $\phi = 0^\circ$ is pointing to the Sun. The Sun is marked with a yellow dot, the Galactic center with a black dot. Each sector is shown with a different color and is analyzed in panel (B). The dotted line on the disk separates parts of the Galaxy warped toward negative and positive Z (i.e., the line of nodes). (B) Distribution of Cepheids as a function of the Galactocentric distance R versus distance from the Galactic plane Z in each sector. The range of azimuth for each sector is labeled. Colors correspond to colors of the sectors in (A). Gray lines are positions of the model surface ((C) to (E)) within a given sector. (C to E) Model of the Milky Way warp from three viewing angles. Cepheids are marked with blue dots, the gray grid is a model surface fit to the Cepheid distribution (10). Cartesian Galactic coordinate system (X, Y, Z) is defined in (10). Vertical distances have been exaggerated by the choice of axes.

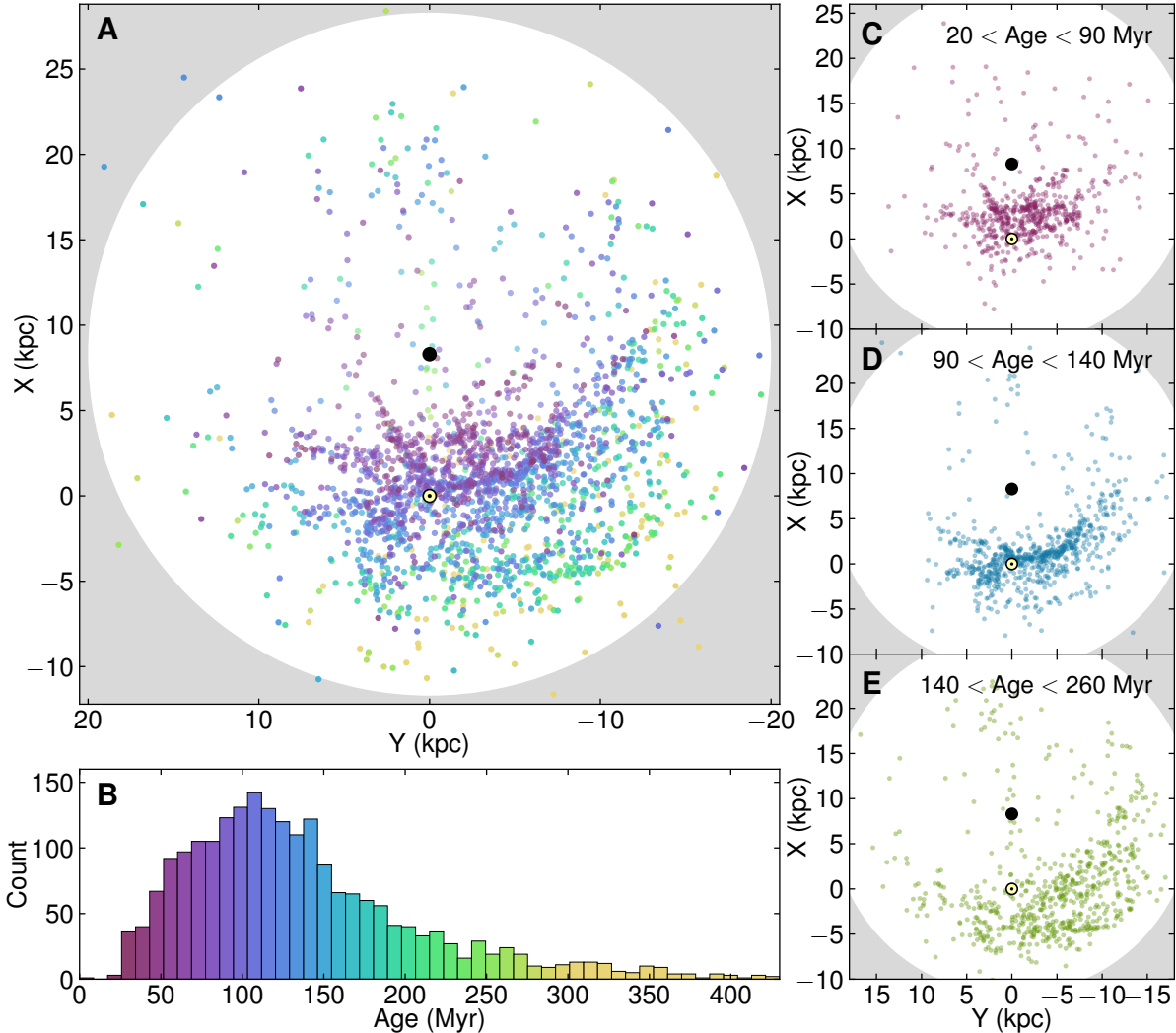


Figure 3: Ages of Galactic classical Cepheids. (A) Face-on view, showing the Cepheid distribution in the Galaxy, with colors corresponding to Cepheid ages as indicated in (B). The Sun is marked with a yellow dot, the Galactic center with a black dot. (B) Age histogram of Galactic classical Cepheids in our sample. (C to E) Age tomography of the Milky Way Cepheids in three selected age bins, as indicated. Each age bin reveals Cepheid overdensities.

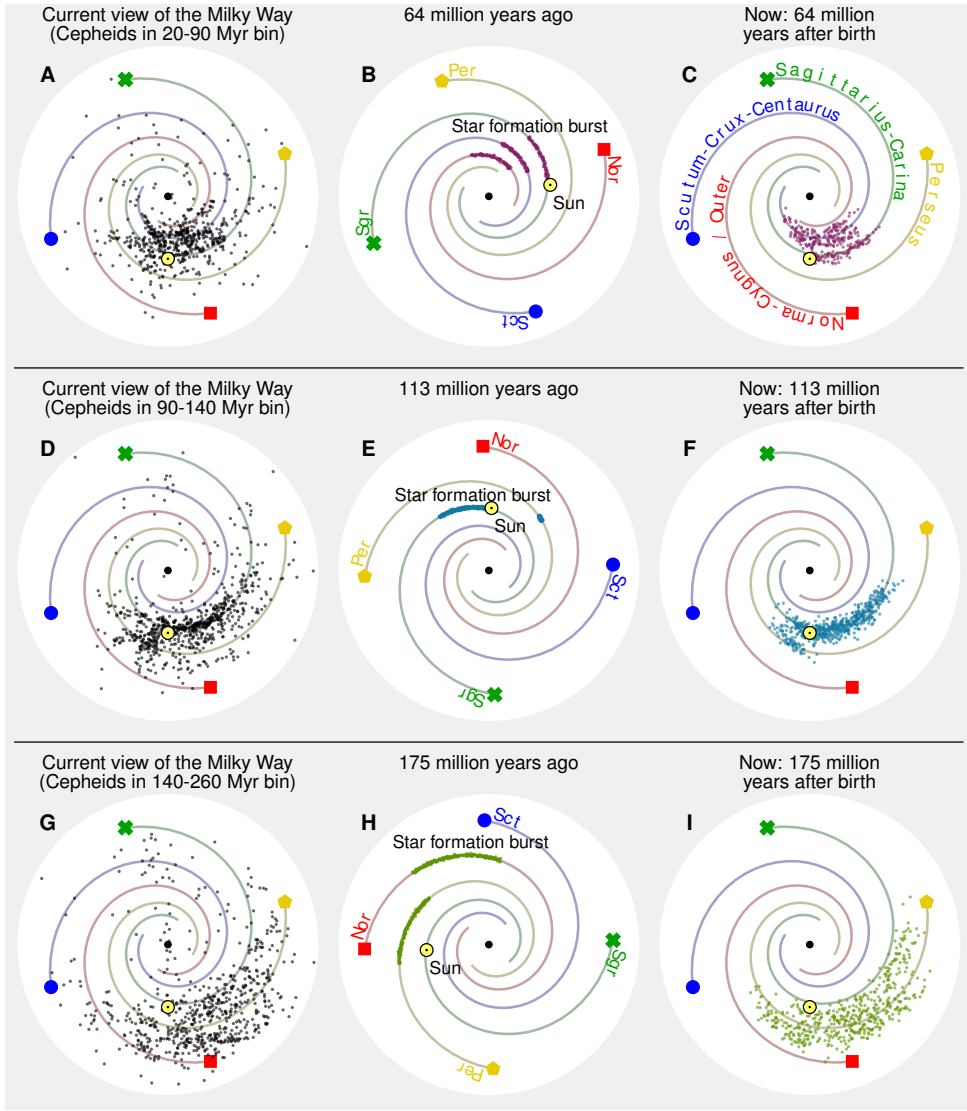


Figure 4: Possible origin of the Cepheid structures. (A) Face-on view of our Galaxy, where Cepheids that belong to the age bin 20 to 90 Myr (median age 64 Myr) are shown with black dots. The Sun is marked with a yellow dot, the Galactic center with a black dot. Locations of the spiral arms: yellow pentagon, Perseus arm; green cross, Sagittarius-Carina arm; blue dot, Scutum-Crux-Centaurus arm; red square, Norma-Cygnus/Outer arm. (B) Location of the Galaxy's spiral arms 64 Myr ago, with simulated star formation regions along the Norma-Cygnus/Outer, Scutum-Crux-Centaurus and Sagittarius-Carina arms marked in violet. (C) Current location of stars from the simulated star formation region (violet). (D to F) Same as (A) to (C), but for the age bin 90 to 140 Myr with a median age of 113 Myr. (G I) Same as (A) to (C), but for the age bin 140 to 260 Myr with a median age of 175 Myr.



Supplementary Materials for

A three-dimensional map of the Milky Way using classical Cepheid variable stars

Dorota M. Skowron, Jan Skowron, Przemek Mróz, Andrzej Udalski, Paweł Pietrukowicz, Igor Soszyński, Michał K. Szymański, Radosław Poleski, Szymon Kozłowski, Krzysztof Ulaczyk,
Krzysztof Rybicki, Patryk Iwanek

Correspondence to: dszczyg@astrouw.edu.pl, udalski@astrouw.edu.pl

This PDF file includes:

Materials and Methods

Figs. S1 to S5

Tables S1 to S2

Other Supplementary Materials for this manuscript include the following:

Data S1

Materials and methods

The Cepheid sample

The sample of classical Cepheids used in this work consists of 2431 objects. The majority (1514 stars) come from the OGLE Collection of Galactic Cepheids (3) (1408 objects from the OGLE-IV Galactic disk and outer Galactic bulge fields (3), 68 objects from the OGLE-IV collection of Galactic bulge Cepheids (31), and 38 objects from the OGLE-III catalog of variable stars in the Galactic bulge (32) and disk (4)). Some of these objects have counterparts in other databases but the majority do not. We also supplement this list with brighter all-sky Cepheids: 592 from the General Catalogue of Variable Stars (GCVS) (5), 61 from the ASAS catalogs (6), and 15 from other sources (Data S1).

The catalog of new variable stars from the ASAS-SN survey (7) contains 315 objects classified as classical (249) or type II (66) Cepheids, together with their V-band light curves. Because the classification procedure of ASAS-SN is mainly automatic, we visually inspected all Cepheid light curves. As a result, we confirmed 147 classical and 43 type II ASAS-SN Cepheids, with a misclassification rate between the original Cepheid types of about 30%. The remaining variable stars are mainly spotted variables, eclipsing binaries, anomalous Cepheids, or RR Lyr type stars. Among 147 classical Cepheids, 50 were already in our sample, so we supplement it with 97 ASAS-SN objects.

We also used the ATLAS project catalog of variable stars (8) to identify classical Cepheids. Following the survey documentation, we selected all stars with the 'PULSE' classification that have a long-period fit or a short-period fit leading to a master period longer than 1 day. We also selected stars that were not classified as 'PULSE' but reveal clear variability, and their master period is longer than 1 day. See (8) for further details. The search resulted in almost 3000

Cepheid candidates with available light curves. Our analysis of the ATLAS time series was similar to the procedures applied to the OGLE photometry. We determined periods, amplitudes, and Fourier coefficients for all available light curves in both passbands (cyan and orange) used by the ATLAS survey. Then, we selected and classified pulsating stars based on the visual inspection of their folded light curves, taking into account their position in the Period–Fourier coefficients diagrams (31, 33) and ratios of the light amplitudes in the two ATLAS filters. The classification procedure returned 438 classical Cepheids, 152 of which were not already in our sample. We also identified 142 type II Cepheids and 61 anomalous Cepheids in the ATLAS Cepheid candidate sample. The majority of the remaining 2130 ATLAS objects turned out to be eclipsing binaries and spotted variables, and even some RR Lyrae type stars that were assigned a 1-day alias period.

The OGLE Cepheid Collection confirms 211 classical Cepheid candidates published in the Gaia DR2 Cepheid sample (9). Four of them were not in the original OGLE catalog (3) but are confirmed with OGLE-IV data. Galactic Gaia DR2 Cepheid candidates located outside of the OGLE sky footprint were not included in our sample due to contamination and low completeness (3).

The full list of 2431 classical Cepheids used in this work is presented in Table S1, including a reference to a discovery paper, whenever available. Otherwise we provide the source (*e.g.*, GCVS) or a database, in which the Cepheid was identified (*e.g.*, ATLAS). For Cepheids from the OGLE Collection that have counterparts in other databases we provide an additional database identifier. Fig. S1 presents the distribution of our Cepheid sample in the Milky Way, coded by the source of data.

MID-IR data

The mid-IR observations of Cepheids were taken by the Wide-field Infrared Survey Explorer (WISE) and the Spitzer Space Telescope.

We utilized the WISE data from the AllWISE Multiepoch Photometry Database, which provides all-sky time-series photometry from both the WISE cryogenic and “Near Earth Object WISE” (NEOWISE) post-cryogenic phases of the survey (34, 35). The observations were made in four bands: W1 (3.4 micron), W2 (4.6 micron), W3 (11.6 micron), and W4 (22.1 micron). We found counterparts for 2068 out of 2431 Cepheids within 1'' search radius. The number of points per light curve in the W1 band varied from 0 to over 301 with a median value of 40 points. We calculated weighted mean magnitudes for 2041, 2055, 1488 and 524 Cepheids in W1, W2, W3 and W4 bands, respectively.

While calculating the weighted mean magnitude, the weight of each data point is taken as an inverse square of the uncertainty reported by the survey (σ_i^{-2}). We assign the uncertainty of the weighted mean by taking three factors into account: the weighted standard deviation of the light curve, the standard error of the weighted mean calculated from the weights $(\sum_i \sigma_i^{-2})^{-1/2}$, and the expected root mean square (rms) scatter of the Cepheid light curve, caused by its pulsations. We found that the uncertainties reported in the catalog are not a reliable indication of the true observational uncertainty in this dataset. The WISE light curve typically covers only a small portion of the pulsational period. Hence, typically, its standard deviation better corresponds to the observational errors than to the pulsational scatter. To be conservative, we decided to use either the weighted standard deviation of the measurements or the standard error of the weighted mean, whichever is greater, and combine it in quadrature with the expected uncertainty originating from pulsations. Using this approach, at the cost of possible minor overestimation of the uncertainty (up to a factor of $\sqrt{2}$), we avoid overconfidence in the mean brightness measurement for many stars.

Since the mid-IR amplitudes for the majority of Cepheids are not known, due to the low number of observations, we use their optical light curves to estimate the expected mid-IR amplitude. Most Cepheids in our sample have well covered *I*-band light curves, so their amplitude and thus the expected rms scatter can be estimated. In the case when only the *V*-band light curve is available, we scale the *V*-band amplitude by a factor of 0.6 to estimate the *I*-band amplitude and rms scatter (36).

We then choose a subset of Cepheids with well sampled light curves for every WISE band. From those, we pick the ones with low photometric noise and estimate their mid-IR rms scatter. We found that the rms scatter in the *I*-band is proportional to the rms scatter in all mid-IR bands with the proportionality constant close to 2. Therefore, we take the measured rms *I*-band scatter, divide it by 2, and use it as a measure of the mid-IR rms scatter.

The measurements from WISE are often grouped in time, as such, all measurements collected in close temporal proximity can be treated as a single-epoch. The estimation of a mean brightness having only one or two measurements across all pulsation phases is uncertain. When we assume that the pulsational light curve is sinusoidal in shape, the uncertainty of the mean as estimated from a single-epoch measurement can be taken as 0.7 of the rms scatter, and as estimated from two epochs – 0.5 of it.

Table S1 contains our assessment of the mean magnitudes in all four WISE bands together with the uncertainties we assigned to these measurements.

We also use the data from the “Galactic Legacy Infrared Midplane Survey Extraordinaire” (GLIMPSE) Legacy Program of Spitzer and its extensions: GLIMPSE II, GLIMPSE 3D, GLIMPSE 360, Deep GLIMPSE and Vela-Carina, as well as from the ”Spitzer Mapping of the Outer Galaxy” (SMOG) and ”A Spitzer Legacy Survey of the Cygnus-X Complex” (Cygnus-X) Legacy Programs (37, 38), which we will collectively call the GLIMPSE data. The Spitzer observations of the Galactic plane were made in four Infrared Array Camera (IRAC) bands: I1

(3.6 micron), I2 (4.5 micron), I3 (5.8 micron) and I4 (8.0 micron). For each Cepheid from our final list we extracted all available GLIMPSE observations within 1" search radius. We found matches for 1247 out of 2431 objects. The majority of Cepheids (980) had only one match in the GLIMPSE catalogs, while 267 were found in more than one GLIMPSE programs: 234 stars had 2 matches, 31 stars had 3 matches and 2 stars had 4 matches. We calculated mean magnitudes for 1121, 1154, 772 and 731 Cepheids in I1, I2, I3 and I4 bands, respectively.

The number of data points in each light curve is very limited, and the majority of objects have one or two measurements. For objects with only one measurement, we take its value as an approximation of the mean magnitude and attach the uncertainty based on two factors: the reported uncertainty of the data point, and the expected rms scatter based on the pulsation amplitude multiplied by 0.7. For objects with two or more data points, we use the standard error of the weighted mean and the rms of pulsation multiplied by 0.5. The results are presented in Table S1.

Distances and extinction

The distance d in a given band λ can be calculated as:

$$d_\lambda = 10^{0.2(m_\lambda - M_\lambda - A_\lambda)+1} \text{ pc} \quad (\text{S1})$$

where m_λ and M_λ are, respectively, the observed and absolute magnitudes of the star and A_λ is the extinction value. The absolute magnitudes can be calculated from the P-L relations. Here we use the mid-IR P-L relations derived for the Spitzer and WISE passbands (*I1*) based on a sample of 288 Galactic classical Cepheids. The extinction values in the Galaxy are high in the optical bands and vary strongly between lines-of-sight, but become much lower in the mid-IR. Nevertheless, in some directions, especially close to the Galactic plane or in the Galactic bulge, the mid-IR extinction can be large. Therefore, we assess its value for each individual Cepheid.

We used the 3-D map of interstellar extinction “mwdust” (39) that provides extinction in the requested band (in our case K_s) for the Galactic coordinates (l, b) and the distance d from the Sun. The map contains two merged 3-D maps. For the highly extincted part of the Galaxy ($-100^\circ < l < 100^\circ$) it uses the map of ref. (19) based on “Two Micron All-Sky Survey” (2MASS), and for the remaining longitudes the Bayestar15 map (40) based on “Panoramic Survey Telescope And Rapid Response System” (Pan-STARRS) and 2MASS. The former map samples the extinction up to 12–15 kpc from the Sun. The vast majority of Cepheids are located within that range, but for single objects the extinction may be slightly underestimated because of neglecting residual reddening in the outskirts of the Galaxy. The extinction map of ref. (40) has a shorter range (5–6 kpc), but it is used in the directions of lower reddening, where Cepheids are located much closer. Again, the extinction may be slightly underestimated for some Cepheids located farther than 6 kpc in these directions.

To make sure that our IR extinction values from “mwdust” maps are reliable, especially in the lines-of-sight with higher extinction, we conducted an additional test. We tried to derive A_{K_s} for each individual Cepheid using its multiband IR photometry. The mid-IR extinction curve is fairly flat, so the mid-IR photometry alone is insufficient for this purpose, and at least a K_s -band measurement is necessary to have an estimate of A_{K_s} . We used the “VISTA Variables in the Via Lactea” (VVV) survey data (41) and extracted K_s -band photometry for a sample of our Cepheids. For the objects having more than 7 epochs, we calculated their mean intensities. Then assuming the mid-IR extinction curve (42) (i.e., extinction ratios $R_i = A_i / A_{K_s}$) and the mid-IR photometry we derived the most likely extinction A_{K_s} and extinction-corrected distance modulus μ_0 , by solving a set of linear equations $(m - M)_i = \mu_0 + R_i \times A_{K_s}$, for 273 objects. The accuracy of this measurement strongly depends on the K_s value obtained from the VVV aperture photometry.

Generally, these A_{K_s} values and the ones from “mwdust” are consistent, which is reassuring. On average, the “mwdust” extinction value is only slightly lower (by 0.05 mag) albeit the dispersion of A_{K_s} measurements (0.5 mag) is large. Because of the strong dependence of the accuracy of the extinction determination on the Cepheid K_s photometry, we conclude that the “mwdust” extinction value is more reliable and homogeneous and thus, we use it in the distance determination.

The distances to each object can be derived separately for every available Spitzer and WISE band and then averaged. We take the extinction-corrected distance moduli ($\mu_{0,\lambda} = m_\lambda - M_\lambda - A_\lambda$) and calculate their weighted average with 3σ outlier rejection, and from this calculate the final distance. The mean-brightness uncertainty is added to the relevant P-L relation scatter (11) in quadrature and the weights are set as inverse squares of these values. The standard deviation of the weighted mean of the distance modulus (σ_μ) propagates to the final distance uncertainty as $\sigma_d = d \times \ln(10) \times 0.2\sigma_\mu$.

When averaging the distances, we found that some portion of rejected measurements comes from the W3 and W4 bands that yield systematically lower distances. Stars for which this happens often have complete set of good measurements in shorter wavelengths (W1 or W2) from all WISE visits, but only a handful of measurements in longer wavelengths (W3 or W4). We take this as an indication of an unreliable measurement in a given band and discard it whenever the number of useful epochs is smaller than 20% of all visits. This procedure lowers the number of outliers we have to reject and helps to better estimate distances for both faint, distant stars (with unreliable W3 and W4 measurements), and also to bright, close-by stars, which are saturated in shorter mid-IR bands, and their distances are usually determined solely from the W3 and W4 bands.

The final distance and the estimated extinction are correlated. We use simple iterations to converge on the final values. First, we calculate the initial distance assuming no extinction.

Then the A_{K_s} is extracted from the “mwdust” maps for a given location (l , b , d) and converted to mid-IR extinction using the mid-IR extinction curve based on results from the “Apache Point Observatory Galactic Evolution Experiment” (APOGEE) survey (42) ($A_{I1}/A_{K_s} = 0.553$, $A_{I2}/A_{K_s} = 0.461$, $A_{I3}/A_{K_s} = 0.389$, $A_{I4}/A_{K_s} = 0.426$, $A_{W1}/A_{K_s} = 0.591$, $A_{W2}/A_{K_s} = 0.463$, $A_{W3}/A_{K_s} = 0.537$, $A_{W4}/A_{K_s} = 0.364$). The extinction-corrected distances in all bands are averaged as described above. We use the new distance d to extract the new value of A_{K_s} extinction from the “mwdust” maps. After a couple of iterations, the process converges.

Table S1 provides Galactic coordinates (l , b), the final distance value and its uncertainty, estimated age, pulsation period and mode, mean magnitudes in all eight mid-IR bands and their estimated uncertainties (Data S1 only), as well as near-IR extinction A_{K_s} , for all Cepheids in our sample.

Having the final distances obtained with the optimized mid-IR extinction, we verified their reliability. Our distances were compared with distances from the Gaia DR2 sample (43), by selecting counterparts with parallax errors $<10\%$. 251 common objects were found. The comparison indicates the presence of a bias in the Gaia parallaxes of -0.071 ± 0.038 mas (30). Ref. (44) noted such a bias at the level of -0.046 ± 0.013 mas in their Cepheid sample. Other comparisons: quasars (45), RGB stars (46), eclipsing binaries (47), RR Lyrae stars (48) also suggest a bias of the Gaia DR2 distance scale at a similar level (from -0.030 to -0.082 mas). Thus, our distance scale seems to be compatible with current distance scale determinations. Even if our distance scale is slightly incorrect, our picture of the Milky remains the same – it will just be somewhat rescaled.

The Gaia Cepheids are nearby objects. Ref. (49) measured distances and extinction to five OGLE Cepheids from independent JK photometry. These objects are located ≈ 15 kpc behind the Galactic center and are seen through high extinction. We have the mid-IR photometry

for only one of these objects, namely OGLE-BLG-CEP-005. Our distance to this object is 23.06 ± 0.77 kpc while ref. (49) gives 22.30 kpc. The agreement to 3% is reassuring and suggests that our distance scale is precise at large distances as well.

These tests indicate that our distance scale is accurate to better than 5%.

Cartesian coordinates

The 3-D distribution of Cepheids in our sample is studied in the Cartesian coordinate system with the origin at the Sun:

$$\begin{aligned} X &= d \times \cos l \cos b \\ Y &= d \times \sin l \cos b \\ Z &= d \times \sin b \end{aligned} \tag{S2}$$

where l and b are the Galactic coordinates of the star and d is its distance from the Sun. We adopt the distance between the Galactic center and the Sun of 8.3 kpc (50, 51).

Galactic warp

The 3-D distribution of Cepheids deviates from a plane. To guide the eye, we fitted a simple polynomial surface to the distribution of Cepheids:

$$\begin{aligned} Z(R, \phi) &= -z_0 && \text{for } R < R_d \\ Z(R, \phi) &= -z_0 + z_1(R - R_d)^2 \sin(\phi - \phi_0) && \text{for } R \geq R_d \end{aligned} \tag{S3}$$

where z_0 is the distance of the Sun from the Galactic plane, z_1 – warp amplitude parameter, R_d – the distance from the Galactic center where the warp begins and ϕ_0 – azimuth of the line of nodes.

We find the best-fitting parameters by minimizing the sum of squares of orthogonal distances from the data points to the surface $\chi^2 = \sum_i \|\vec{R}_i - \vec{R}_{\text{model}}\|^2$. The best-fitting parameters are $z_0 = 15.3$ pc (in good agreement with the Sun's height from the thin disk exponential model –

see below), $z_1 = +0.0152 \text{ kpc}^{-1}$ and $\phi_0 = -28^\circ$ for fixed $R_d = 8 \text{ kpc}$. The best-fitting surface is shown in Fig. 2 C, D, E.

We can see the Galactic warp in our 3-D map of the Galaxy using directly measured distances to individual stars. Previous studies were mostly based on star counts (14–18), distribution of red clump stars (15, 16) and pulsars (52), distribution of dust (19) and gas (12, 13) or stellar kinematics (20, 21). Our map is a global approach – based on observations of Cepheids in the entire Galaxy – far from the Galactic center, and not only in the regions relatively close to the Sun.

Previous models do not match the shape of the Galactic warp as seen in classical Cepheids. Models of the warp that assume a linear shape (17–19) are likely excluded, as our data show that the inclination of the warp is not constant (Fig. 2 B). The height of the warp in the intermediate-age population ($1.7 - 1.8 \text{ kpc}$ at $R = 15 \text{ kpc}$) (14, 15) is much higher than for Cepheids (0.74 kpc at $R = 15 \text{ kpc}$). The position angle of the line of nodes of the warp is $\phi_0 = -28^\circ$ for Cepheids (Fig. 2 A), while it is closer to zero for older stars (14, 15). This may indicate that the shape of the warp differs between the young and older stellar populations (as also suggested by ref. (18)).

Fig. 2 also excludes the interpretation of far disk Cepheids by ref. (49). They were unaware of the large warping of the disk toward positive latitudes in the direction of the Galactic center ($165^\circ < \phi < 210^\circ$). Therefore, the location of these Cepheids is typical – in the middle of the disk – not at the ~ 3 -sigma edge of the flaring disk.

To illustrate the flaring of the disk, we divided it into 10 equal sectors in the Galactocentric polar coordinate system (similar to those in Fig. 2), calculated the median Z in 20 bins in Galactocentric radius (provided that the bin contained at least five stars), and subtracted the median warping. The results are shown in Fig. S2, which presents the cross-section of the entire disk in the young population. We found that the thickness of the disk seen in classical Cepheids is in agreement with observations of atomic hydrogen (22).

Disk scale height

We model the vertical distribution of Cepheids using a simple exponential model of the thin disk, which has two free parameters: the scale height H and the Sun's height above the Galactic plane z_0 . The density of stars varies as:

$$n(z) = \frac{1}{2H} \exp\left(-\frac{|z|}{H}\right) \quad (\text{S4})$$

where $z = z_0 + d \sin b$, d is the distance to the Cepheid and b is its Galactic latitude. The best-fitting model is found by maximizing the likelihood function, \mathcal{L} , defined as $\ln \mathcal{L} = \sum_i \ln n(z_i)$. The summation is performed over all stars within 8 kpc of the Galactic center (to minimize the effect of the disk's warp) and Galactic latitudes $|b| \leq 4^\circ$. The best-fitting parameters are $H = 73.5 \pm 3.2$ pc and $z_0 = 14.5 \pm 3.0$ pc. The uncertainties are estimated using the Markov chain Monte Carlo technique (53) and represent 68% confidence range of marginalized posterior distributions. We assume uniform priors on H and z_0 over the ranges 0 to 1 kpc and -1 to 1 kpc, respectively.

The estimated mean scale height is consistent with our measurements of flaring of the disk (Fig. S2), as the mean HWHM = $H \ln 2 = 51$ pc. The measured parameters are in general agreement with previous determinations (Table S2). The histogram of distance z together with the fit model is presented in Fig. S3.

Period–Galactocentric Distance Distribution

Fig. S4 shows the distribution of periods of fundamental mode Cepheids from our sample as a function of the Galactocentric distance. A clear decrease of the minimum Cepheid period with the distance implies a radial metallicity gradient in the Milky Way. The metallicity gradient is also directly observed in Cepheid spectra (25). Less massive stars in more metal rich environments cannot reach the Cepheid instability strip in the helium-burning phase of evolution and cannot appear then as short-period Cepheids (24).

We carried out a simple simulation to check if a constant star formation rate (SFR) can reproduce Fig. S4 at distances $R > 8$ kpc, i.e., covered by available metallicity of models (24, 54). We assumed an exponential distribution of stellar density ($n(R) \propto \exp(-R/H_R)$) in the Galaxy with a scale length $H_R = 3$ kpc and drew stars from this distribution. Metallicities were taken from the metallicity–distance relation (25) and their masses, M , and ages were assigned from the Initial Mass Function (IMF) ($dN/dM \sim M^{-2}$) and flat age distribution in the range of [0, 300] million years. Then, we followed the evolution of each star using evolutionary tracks (54) and if a star of a given mass, metallicity and age was within the instability strip (24), we treated it as a Cepheid. We assigned its present period using the period–age relation (24).

The minimum periods of our simulated Cepheid sample match the observed values: $\log P_{\min} \approx 0.5$ at the distance of $R \approx 9.5$ kpc (solar metallicity of about 0.014), and $\log P_{\min} \approx 0.3$ at the distance of $R \approx 18$ kpc (metallicity of about 0.006). However, there are fewer long-period ($\log P > 0.5$) Cepheids observed in the regions far from the Galactic center ($16 < R < 20$ kpc) than predicted by the simulation. On the other hand, in the regions of solar metallicity ($8 < R < 12$ kpc) we obtain a reverse situation – the number of the observed long-period Cepheids ($\log P > 0.8$) is higher than in the simulations (Fig. S5). These results indicate that our assumption of constant SFR is likely not correct. Moreover, the simulated SFR per unit volume in the outer parts of the Galaxy would need to be lower by a factor of 4 – 5 than in the solar neighborhood to match the observations. This conclusion is in agreement with the SFR estimated from the distribution of molecular gas (55).

Age of Galactic Cepheids

The age of a classical Cepheid is correlated with its period and the Period-Age relation depends on metallicity (56). Models show that this relation also depends on the rotation of the star (24). The rotation increases the age of Cepheids by a factor of up to two. We used the Period-Age

relations (24) to derive ages of Galactic Cepheids from our sample. Because the progenitors of classical Cepheids – B/A-type main sequence stars – are typically fast rotators (57, 58) we assumed the Period-Age relations for $\omega = 0.5$ (where ω is the ratio of the initial angular velocity of the star to the critical one). For a wide range of rotation values – from moderate to very fast ($0.4 < \omega < 0.9$), i.e., applicable to the Cepheid progenitors, the Period-Age relations are almost identical in the Galactic metallicity range ((24), their figure 10).

Unfortunately, the available models and relations (24) were calculated for only three metallicities: solar (0.014), the Large Magellanic Cloud (0.006) and the Small Magellanic Cloud (0.002). However, many Galactic Cepheids are more metal-rich than the Sun. Thus, we first extrapolated the relations from ref. (24) to metallicity of 0.030 to cover the full range of Galactic Cepheid metallicities. Over the whole range of Cepheid periods the more metal-rich Cepheids are younger than the less metal-rich ones at the same pulsation period.

There is a radial metallicity gradient in the Galaxy (25). For each Cepheid from our sample we estimated its typical metallicity based on the distance R from the center. Then we applied the appropriate (for fundamental-mode or first-overtone pulsations and $\omega = 0.5$) Period-Age relation (24) to derive its age.

Results of our age determination for Galactic Cepheids are presented in Fig. 3 A where the age tomography of the Milky Way Cepheids is plotted and Fig. 3 B shows the distribution of ages of Cepheids from our sample.

Modeling the overdensities

We divide the Cepheid sample into three age bins: young (20–90 Myr), intermediate (90–140 Myr), and old (140–260 Myr) – Fig. 3 C–E. The median ages of stars falling into the marked regions are 64, 113, and 175 Myr, respectively, and standard deviations are 16, 14, 33 Myr. The two youngest bins show a couple of narrow overdensities with similar ages.

Because our age estimates are not accurate, we expect that stars that formed together might show slightly different ages. However, the spatial positions are known with much better accuracy. Thus, close spacial proximity of stars of similar age strongly suggests their common origin and indicates a small relative-velocity dispersion.

We model the overdensities in those three bins, assuming a single age for all stars inside the bin. Disk stars in the Galaxy follow a flat rotation curve with the velocity of 223 km/s (30). We take the rotational period of the spiral pattern equal to 250 Myr (29). The age bins are illustrated in Fig. 4 A, D, G. For each age group, we pick regions within neighboring spiral arms, populate them randomly with stars and assign them the rotation velocities with an additional (8, 8) km/s dispersion in the (U , V) directions. Positions of these Cepheid candidates are shown in Fig. 4 B, E, H. Rotation of the Galaxy to the present day is shown in Fig. 4 C, F, I. We use a simple four-arm spiral structure model with a pitch angle of 12.4 degrees (29, 59).

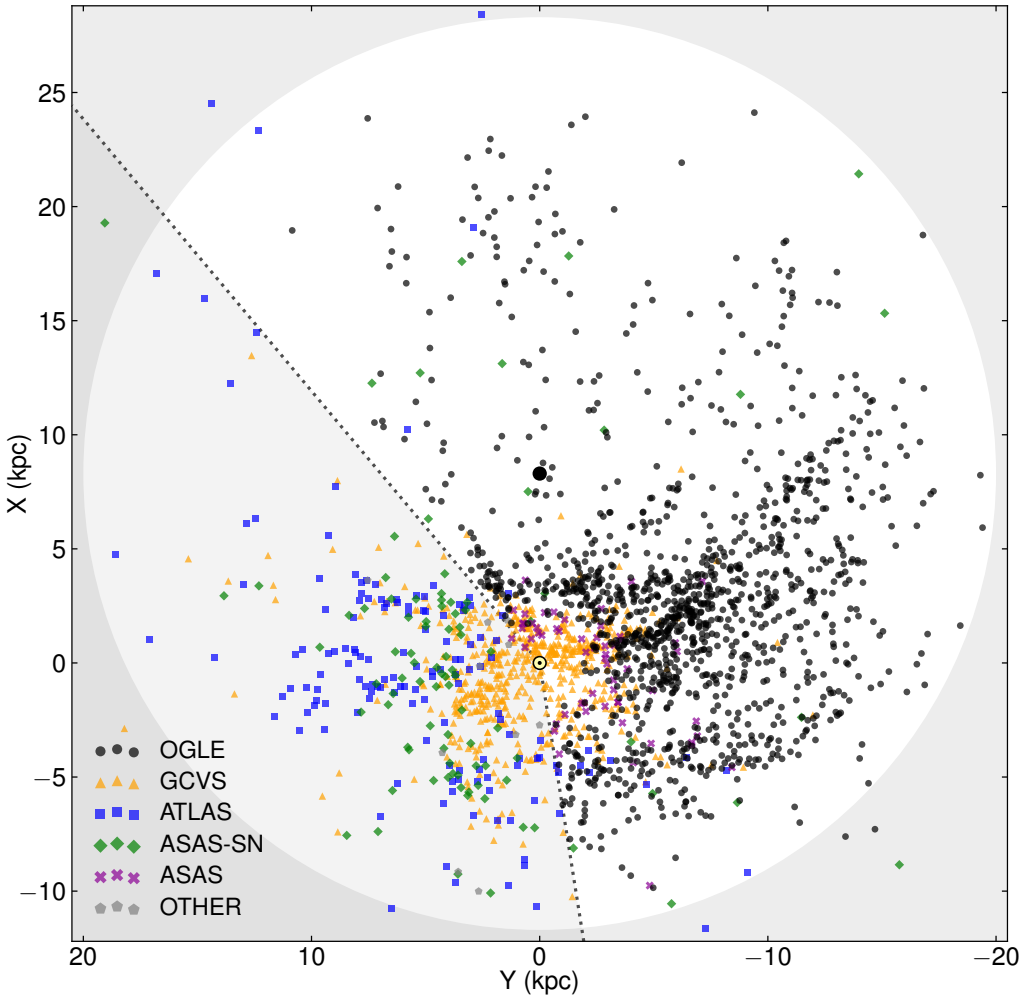


Figure S1: Distribution of Galactic classical Cepheids from different databases. Same as Fig. 1 B, but indicating the source of each Cepheid on a plain background. See text for details of the sources.

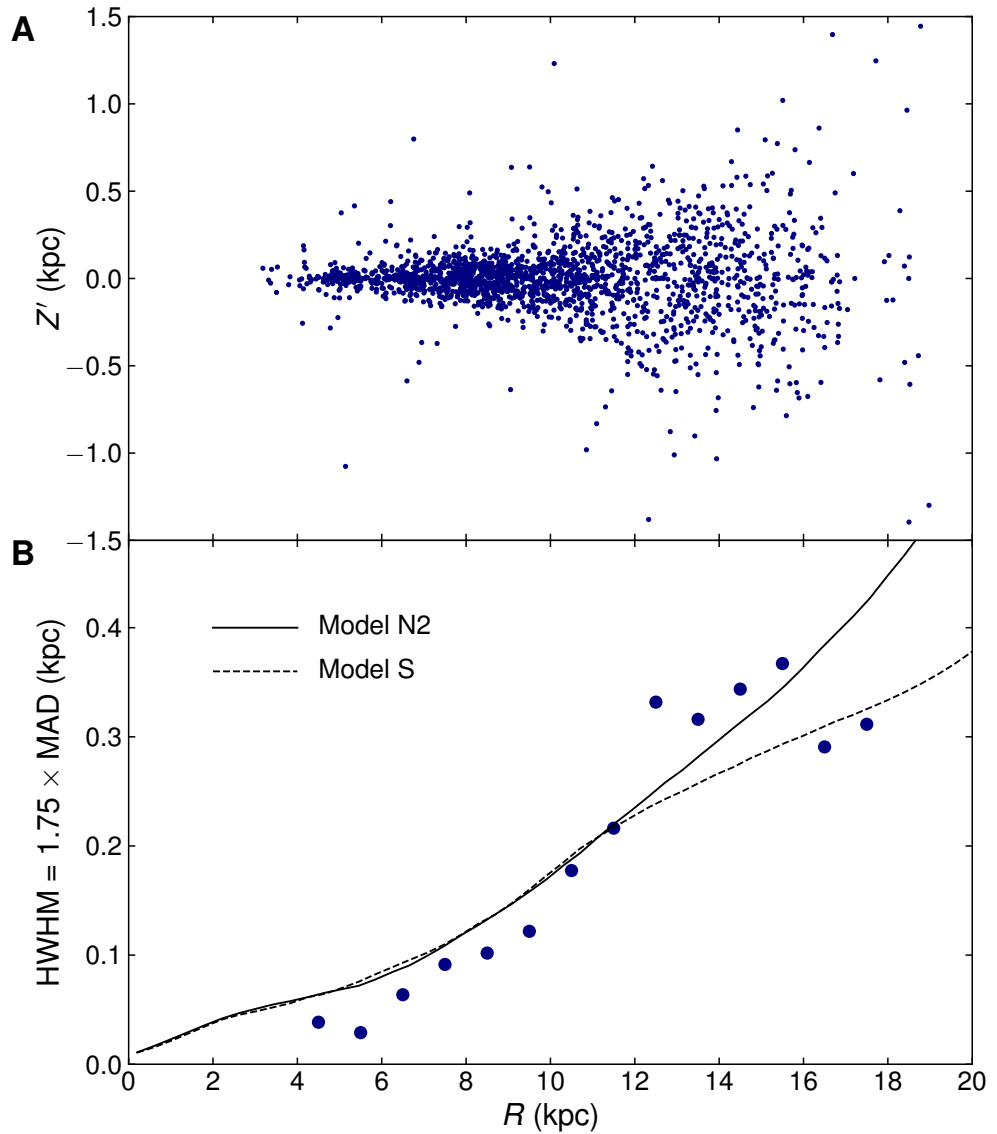


Figure S2: Flaring of the Galactic disk in classical Cepheids. **(A):** Cross-section of the Galactic disk after subtracting the median warping ($Z' = Z - \text{median warping}$). **(B):** Thickness of the flaring disk as a function of the Galactocentric radius (MAD is the median absolute deviation and HWHM the half-width at half-maximum). Dots represent the investigated Cepheid sample. Solid and dashed lines show models of flaring of the northern (N2) and southern (S) part of the disk, based on radio observations of atomic hydrogen (22).

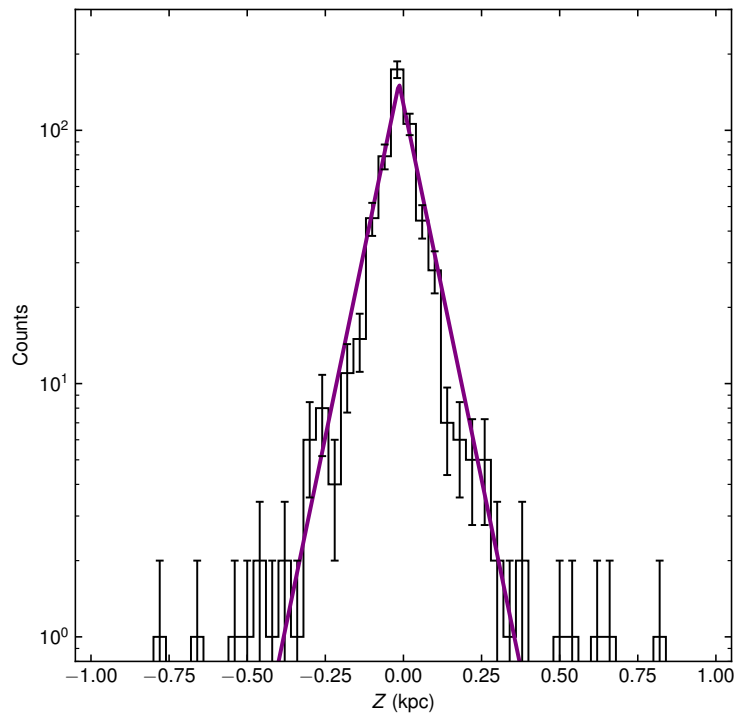


Figure S3: Histogram of distances of Cepheids from the Galactic plane. Histogram for objects located within 8 kpc of the Galactic center and $|b| \leq 4^\circ$. The purple line marks the best-fitting exponential model.

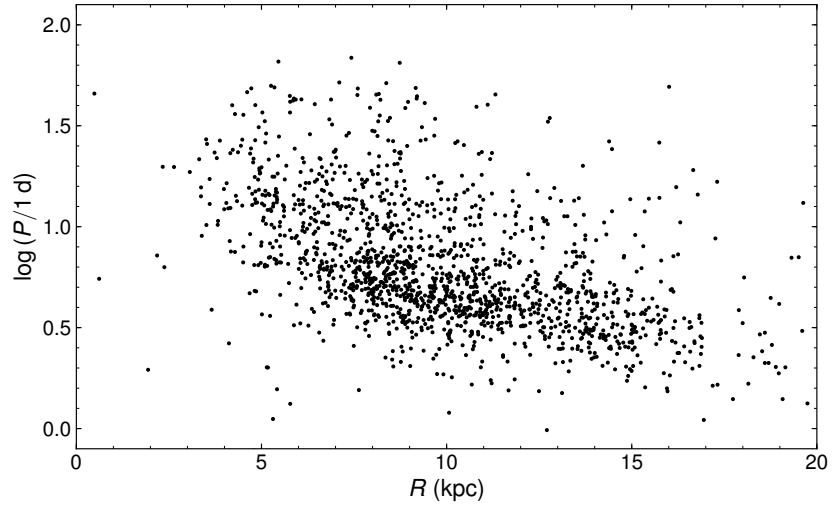


Figure S4: Distribution of periods of fundamental mode classical Cepheids in the Milky Way as a function of the Galactocentric distance.

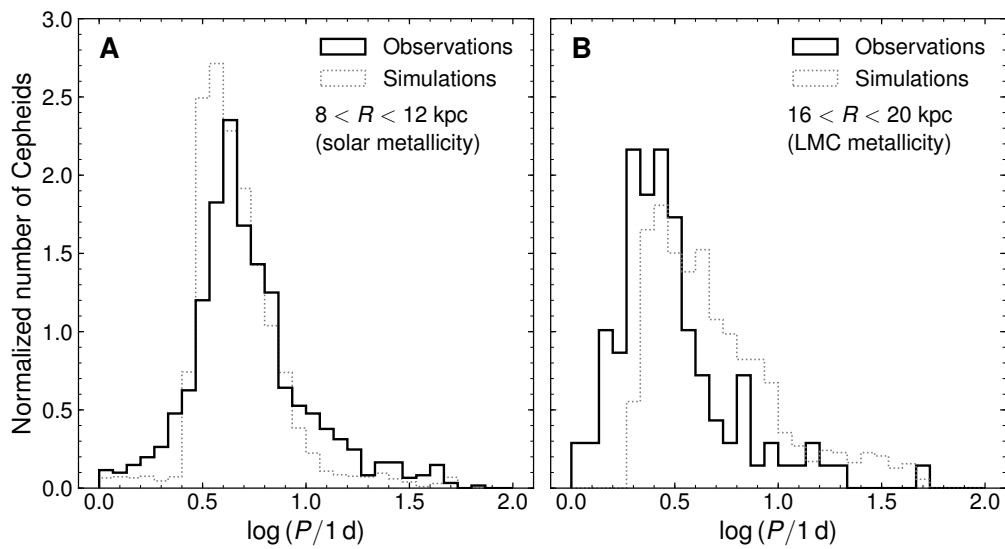


Figure S5: Observed and simulated distribution of periods of classical Cepheids in the Milky Way, assuming a constant star formation rate. Panel (A) shows the distribution of periods at the solar distance (metallicity equal to 0.014) while the panel (B) – at the outskirts of the Milky Way (metallicity equal to 0.006).

Table S1: Classical Cepheid sample. The following columns contain: (1) Source (references only in Data S1 table), (2) Cepheid ID, (3,4) Galactic coordinates, (5,6) distance to the Cepheid and its error in pc, (7) Cepheid age in Myr, (8) Pulsation period in days, (9) Pulsation mode: fundamental (F), first-overtone (1O), (10–13) Spitzer photometry, (14–17) WISE photometry, (18) interstellar extinction in the K_s -band, (19) Source “–”: OGLE Galactic Cepheid Collection star in other databases. “–1” denotes unavailable/missing data. The full Table S1 (2431 Cepheid entries) is available as Data S1 table. Errors of Spitzer and WISE magnitudes are available only in Data S1 table.

Source	Cepheid ID	l (deg)	b (deg)	d (pc)	σ_d (pc)	Age (Myr)	Period (d)	Mode	II (mag)	12 (mag)	13 (mag)	14 (mag)	W1 (mag)	W2 (mag)	W3 (mag)	W4 (mag)	A_{K_s} (mag)	Source “”			
OGLE-IV	OGLE-BLG-CEP-065	0.141777	1.28542	19331	865	130	4.5186140	F	12.202	12.174	12.209	11.801	-1.000	-1.000	-1.000	-1.000	0.670	—			
OGLE-II	OGLE-BLG-CEP-018	0.24164	-2.67713	-1	0	101	2.8467837	F	-1.000	-1.000	-1.000	-1.000	-1.000	-1.000	-1.000	-1.000	-1.000	—			
OGLE-IV	OGLE-BLG-CEP-078	0.24164	-1.30227	-1	0	359	0.3247108	10	-1.000	-1.000	-1.000	-1.000	-1.000	-1.000	-1.000	-1.000	-1.000	—			
OGLE-IV	OGLE-BLG-CEP-063	0.335451	1.67398	18326	1254	217	1.3795193	10	13.286	12.977	-1.000	-1.000	-1.000	-1.000	-1.000	-1.000	-1.000	0.510	—		
OGLE-IV	OGLE-BLG-CEP-059	0.338447	1.96189	6275	555	249	0.3494682	10	12.754	13.160	12.653	-1.000	-1.000	-1.000	-1.000	-1.000	-1.000	-1.000	0.445	—	
OGLE-IV	OGLE-BLG-CEP-098	0.470760	-6.65564	-1	0	267	0.6706328	F	-1.000	-1.000	-1.000	-1.000	-1.000	-1.000	-1.000	-1.000	-1.000	-1.000	—		
OGLE-IV	OGLE-BLG-CEP-058	0.502423	2.11348	20887	696	113	0.4882058	10	11.656	11.765	11.702	11.745	-1.000	-1.000	-1.000	-1.000	-1.000	0.513	—		
OGLE-IV	OGLE-BLG-CEP-082	0.78516	-1.25514	-1	0	154	1.1074519	10	-1.000	1.000	-1.000	-1.000	-1.000	-1.000	-1.000	-1.000	-1.000	-1.000	—		
OGLE-III	OGLE-BLG-CEP-024	0.92608	-3.41198	1.1050	653	247	0.3554251	10	13.901	13.982	-1.000	-1.000	-1.000	-1.000	-1.000	-1.000	-1.000	-1.000	0.201	—	
OGLE-IV	OGLE-BLG-CEP-060	0.93668	2.14174	20429	997	134	0.4386754	F	12.203	12.314	11.972	11.873	-1.000	-1.000	-1.000	-1.000	-1.000	-1.000	-1.000	0.549	—
OGLE-IV	OGLE-BLG-CEP-047	1.01307	3.68211	-1	0	64	3.9657545	10	-1.000	-1.000	-1.000	-1.000	-1.000	-1.000	-1.000	-1.000	-1.000	-1.000	—		
OGLE-IV	OGLE-BLG-CEP-080	1.15305	-0.92199	5022	166	255	0.3328426	10	12.477	12.324	12.411	-1.000	-1.000	-1.000	-1.000	-1.000	-1.000	-1.000	0.464	—	
GCVS	W ₋₋₋ Sgr	1.16628	-0.20926	350	13	306	0.2865322	10	11.787	11.724	11.721	11.572	-1.000	-1.000	-1.000	-1.000	-1.000	-1.000	-1.000	0.072	—
OGLE-III	OGLE-BLG-CEP-019	1.753682	-2.11628	3430	110	224	0.4406742	10	12.866	12.762	-12.537	-1.000	-1.000	-1.000	-1.000	-1.000	-1.000	-1.000	0.306	—	
OGLE-III	OGLE-BLG-CEP-020	1.20440	-2.27310	7518	326	224	0.4406742	10	12.905	12.122	11.880	12.105	-1.000	-1.000	-1.000	-1.000	-1.000	-1.000	-1.000	0.277	—
OGLE-IV	OGLE-BLG-CEP-066	1.49232	1.73999	17634	895	126	0.29816002	10	13.305	13.251	-1.000	-1.000	-1.000	-1.000	-1.000	-1.000	-1.000	0.685	—		
OGLE-III	OGLE-BLG-CEP-027	1.56067	-4.30572	7417	314	269	0.29653274	10	-1.000	-1.000	-1.000	-1.000	-1.000	-1.000	-1.000	-1.000	-1.000	0.147	—		
GCVS	V773-Sgr	1.57578	-3.97156	412	18	85	7.3950300	F	-1.000	-1.000	-1.000	-1.000	-1.000	-1.000	-1.000	-1.000	-1.000	0.024	—		
OGLE-IV	OGLE-BLG-CEP-044	1.753682	-1	0	240	38241	0.3824633	10	-1.000	-1.000	-1.000	-1.000	-1.000	-1.000	-1.000	-1.000	-1.000	-1.000	—		
ASAS	J17528-2736.1	1.97820	-0.70002	1309	32	107	4.8224613	F	-1.000	-1.000	5.946	5.927	5.786	5.818	5.959	5.729	5.729	0.171	—		
OGLE-IV	OGLE-BLG-CEP-076	2.03608	0.10207	3184	70	66	10.3209261	F	7.301	7.168	7.130	7.133	7.209	7.254	7.322	6.165	1.056	—			
OGLE-III	OGLE-BLG-CEP-021	2.07174	-1.87113	13081	633	262	0.37775541	F	13.661	13.604	-1.000	-1.000	-1.000	-1.000	-1.000	-1.000	-1.000	0.351	—		
OGLE-IV	OGLE-BLG-CEP-068	2.15543	1.67911	0	0	327	0.3716363	10	-1.000	-1.000	-1.000	-1.000	-1.000	-1.000	-1.000	-1.000	-1.000	—			
OGLE-IV	OGLE-BLG-CEP-074	2.323318	0.80838	17226	753	142	3.3794859	F	12.564	12.391	12.164	-1.000	-1.000	-1.000	-1.000	-1.000	-1.000	-1.000	0.960	—	
OGLE-III	OGLE-BLG-CEP-029	2.45691	-1.43825	-1	0	114	0.3760846	F	-1.000	-1.000	-1.000	-1.000	-1.000	-1.000	-1.000	-1.000	-1.000	-1.000	—		
OGLE-IV	OGLE-BLG-CEP-094	2.45691	-1.72783	-1	0	330	0.3678108	10	-1.000	-1.000	-1.000	-1.000	-1.000	-1.000	-1.000	-1.000	-1.000	-1.000	—		
OGLE-IV	OGLE-BLG-CEP-072	2.658930	1.43651	9920	442	213	0.4918163	10	13.392	13.299	-1.000	-1.000	-1.000	-1.000	-1.000	-1.000	-1.000	-1.000	0.507	—	
GCVS	V773-Sgr	2.82332	-0.57200	1479	41	96	5.7484450	F	-1.000	-1.000	6.000	5.996	5.979	5.882	6.162	0.187	—	—	—		
OGLE-IV	OGLE-BLG-CEP-091	3.11136	-1.12969	13209	387	47	19.4385184	F	9.900	9.915	9.717	9.648	-1.000	-1.000	-1.000	-1.000	-1.000	0.325	—		
OGLE-IV	OGLE-BLG-CEP-074	3.23347	2.04078	-1	0	145	1.2101512	10	-1.000	-1.000	-1.000	-1.000	-1.000	-1.000	-1.000	-1.000	-1.000	1.950	—		
OGLE-IV	OGLE-BLG-CEP-067	3.558965	2.99334	20431	660	163	2.6107091	10	12.362	12.429	12.241	12.443	-1.000	-1.000	-1.000	-1.000	-1.000	0.343	—		
OGLE-IV	OGLE-BLG-CEP-092	3.707636	-0.78884	-1	0	56	6.8131847	F	-1.000	-1.000	-1.000	-1.000	-1.000	-1.000	-1.000	-1.000	-1.000	-1.000	—		
ASAS-SN	J180520.08265834.0	3.82312	-2.77481	7536	235	127	0.5136369	10	11.008	11.011	10.783	8.753	8.691	8.281	8.612	0.187	—	—	—		
OGLE-IV	OGLE-BLG-CEP-091	4.12746	3.71181	1353	43	97	3.77797030	F	-1.000	-1.000	-1.000	-1.000	-1.000	-1.000	-1.000	-1.000	-1.000	0.226	—		
OGLE-IV	OGLE-BLG-CEP-073	4.26016	2.18427	22316	1688	228	2.2670656	F	13.249	13.456	13.000	-1.000	-1.000	-1.000	-1.000	-1.000	-1.000	0.434	—		
OGLE-III	OGLE-BLG-CEP-003	4.34633	2.88716	-1	0	177	1.2357274	F	-1.000	-1.000	-1.000	-1.000	-1.000	-1.000	-1.000	-1.000	-1.000	-1.000	—		
OGLE-III	OGLE-BLG-CEP-002	4.56861	4.84939	-1	0	127	2.0255716	F	-1.000	-1.000	-1.000	-1.000	-1.000	-1.000	-1.000	-1.000	-1.000	-1.000	—		
OGLE-IV	OGLE-BLG-CEP-079	4.61665	1.21080	15217	628	50	18.4782769	F	9.727	1.000	9.540	-1.000	-1.000	-1.000	-1.000	-1.000	-1.000	0.756	—		
ASAS	J162526-0941.0	4.84083	26.82556	1734	51	166	1.378285	F	-1.000	-1.000	-1.000	-1.000	-1.000	-1.000	-1.000	-1.000	-1.000	0.082	—		
GCVS	V1828-Sgr	5.28401	-4.10021	16825	941	64	12.9751466	F	-1.000	-1.000	-1.000	-1.000	-1.000	-1.000	-1.000	-1.000	-1.000	—	OGLE		
OGLE-IV	OGLE-BLG-CEP-071	6.28869	3.85637	8954	892	144	1.1533927	10	-1.000	-1.000	-1.000	-1.000	-1.000	-1.000	-1.000	-1.000	-1.000	0.340	GAIA		
OGLE-IV	OGLE-BLG-CEP-149	13.28846	-0.20047	2800	97	60	12.5168351	F	-1.000	-1.000	6.162	6.198	6.147	6.114	6.381	-1.000	0.163	ASAS-SN			
OGLE-IV	OGLE-BLG-CEP-150	14.35262	0.34341	3463	78	64	7.1806422	10	7.244	7.072	7.040	6.973	7.127	7.100	7.359	-1.000	0.504	ATLAS			
...				

Table S2: Comparison of recent determinations of the scale height of the thin disk H and the Sun's height above the Galactic plane z_0 .

Reference	Tracers	H (pc)	z_0 (pc)
This study	Cepheids	73.5 ± 3.2	14.5 ± 3.0
(60)	Sgr A* offset from the Galactic plane		17.1 ± 5.0
(61)	Pulsars	56.9 ± 6.5	13.4 ± 4.4
(62)	Open clusters	64 ± 2	6.2 ± 1.1
(63)	Masers	24.1 ± 0.9	5.7 ± 0.5
(64)	Cepheids	66.2 ± 1.6	16 ± 2
(65)	Magnetars	30.7 ± 5.9	13.5 ± 2.6
(66)	Open clusters	~ 40	18.5 ± 1.2
(67)	Open clusters	58 ± 4	16 ± 4
(26)	Cepheids	$< 70 \pm 10$	26 ± 3
(68)	photometric parallaxes	300 ± 60	25 ± 5
(69)	SDSS star counts	330 ± 3	27 ± 4